Transport in Porous Media
https://doi.org/10.1007/s11242-021-01545-x

Methods for Laser-Induced Fluorescence Imaging of Solute Plumes at the Darcy Scale in Quasi-Two-Dimensional, Refractive Index-Matched Porous Media

Eric J. Roth[1,2] · David C. Mays[3] · Roseanna M. Neupauer[1] · Lauren J. Sather[1,4] · John P. Crimaldi[1]

Received: 10 July 2020 / Accepted: 11 January 2021

Abstract
A spectrum of environmental, industrial, and biomedical processes depends on solute plume spreading in laminar flows within porous media. The literature includes a number of approaches to model solute movement in this context, but fewer techniques are reported to measure it experimentally. To address this gap, this study describes novel experimental methods that permit measurement of solute plume spreading at the Darcy scale using laser-induced fluorescence in a 50 cm × 50 cm × 4 cm quasi-two-dimensional apparatus filled with refractive index-matched porous media. Fluorescence is provided by Rhodamine dye; refractive index matching is provided by borosilicate glass in glycerin. The depth-averaged porosity distribution of the porous media is determined using a novel optical method, whose results are used to investigate solute transport in two spatiotemporally varying flow fields, (1) a push–pull pumping sequence and (2) a sequence to induce stretching and folding of the solute plume. Quantitative analysis of replicate experiments reveals an extraordinary degree of reproducibility based on spatial moments, reactor ratio, and correlation coefficient.

Keywords Porous media · Spreading · Mixing · Wall effects · Porosity mapping · Laser-induced fluorescence · Refractive index matching

✉ Eric J. Roth
eric.roth@colorado.edu

[1] Department of Civil, Environmental, and Architectural Engineering, University of Colorado Boulder, Boulder, CO, USA

[2] Present Address: Department of Bioengineering, University of Colorado Anschutz, Denver, CO, USA

[3] Department of Civil Engineering, University of Colorado Denver, Campus Box 113, Denver, CO, 173364, 80217-3364, USA

[4] Present Address: Wildermuth Environmental Inc, Lake Forest, CA, USA

Published online: 02 February 2021

1 Introduction

Flow and transport processes in porous media continue to be important areas of study with applications to a variety of scientific endeavors including fixed-bed reactor design, hydrocarbon development, mineral recovery, biomedical research, and others. Improved knowledge of these processes is imperative for the optimization of groundwater remediation strategies, including in situ remediation techniques, which require the mixing of reactants within the contaminated porous media. A few laboratory experiments have been conducted to investigate the processes that control mixing in porous media (Chen and Wada 1986; Muhammad and Massimo 2017; Stohr et al. 2003); however, porous media experiments are hampered by the lack of optical access within the inherently opaque porous media (Budwig 1994).

To remedy this limitation, many modern transport experiments have built from the pioneering work of Saleh et al. (1992) and Northrup et al. (1993), by employing refractive index-matched (RIM) porous media to gain optical access (Amini and Hassan 2012; Edery et al. 2015; Patil et al. 2014; Roth et al. 2015; Werth et al. 2010; Wright et al. 2017). By matching the refractive index of the porous media with that of the pore fluid, the media/fluid system becomes essentially transparent, allowing the use of advanced imaging techniques including laser-induced fluorescence (LIF) (Amini and Hassan 2012; Chen and Wada 1986; Fort et al. 2015; Stohr et al. 2003; Wright et al. 2017). Advantages of LIF in RIM include in situ, real-time, noninvasive measurements and the ability to probe inner regions of the porous media, which are beyond the influence of wall effects (Roth et al. 2020).

Transport and mixing in porous media are influenced by pore-scale behavior of solutes. Several recent studies report experiments to investigate pore-scale transport of solutes using RIM porous media and fluid to gain optical access (Saleh et al. 1993; Stohr et al. 2003; Kree and Villermaux 2017). In these studies, flow was uniform and one-dimensional, and the pore-scale tracer movement was tracked in multiple dimensions.

In a practical setting, solute plumes in groundwater are many orders of magnitude larger than the pore scale, from meters to kilometers. Therefore, in applications such as design of an in situ remediation system for contaminated groundwater, an understanding of solute transport on a larger scale is necessary. While pore-scale processes still are critical to the overall solute movement, the solute transport behavior must be upscaled to the scale of the plume so that modeling the plume movement is tractable.

This study reports experimental methods that were used to investigate solute movement at the Darcy scale in spatiotemporally varying velocity fields, typical of active spreading protocols for in situ remediation of contaminated groundwater. These experiments are a first step in bridging the gap between experiments that investigate solute transport on the pore-scale and the need for an understanding of plume movement at the field scale. Two key differences between our experiments and those of Stohr et al (2003) and Kree and Villermaux (2017) are the sampling scale and the flow fields. We are interested in the Darcy scale behavior, so we sample the solute concentration over many pores, which is consistent with the way that solute concentrations are measured in the field setting. Furthermore, we investigate solute movement under spatially and temporally varying flow fields. As such, new experimental methods were developed in this study to carry out these experiments. This study reports on improved experimental techniques using LIF in RIM porous media that were developed to evaluate the effects of induced temporally and spatially varying velocity fields on solute transport. The experiments were conducted using RIM

porous media in a quasi-two-dimensional apparatus containing five injection/extraction wells. The improvements over other RIM and LIF experiments allowed for nearly homogeneous porous media packing, mitigation of wall effects, optical access with fine resolution and minimal optical distortion, and a method for determining depth-averaged porosity within the experimental apparatus. Accuracy and precision of these methods are evaluated through replicate experiments.

2 Methods

Several laboratory experiments were conducted to investigate the movement of solute in porous media due to active spreading, which is defined as the manipulation of plume geometry by imposed temporally and spatially varying flow fields. In the experiments, the imposed flow fields were created by a sequence of injections and extractions of fluid in five wells. Throughout the pumping sequence, the solute concentration was imaged at regular time intervals using LIF. This section describes the apparatus, materials, and the procedure for conducting the experiments and the methods used to analyze experimental data.

2.1 Materials and Procedures

The experimental setup (Fig. 1) includes a quasi-two-dimensional apparatus filled with porous media and pore fluid, which contains five ports (wells) for the injection of fluorescent dye (solute) and pore fluid. These ports are connected to a fluid handling system comprising five syringe pumps, supply reservoirs, and waste reservoirs (Supplemental Information Fig. S1). A laser is used to stimulate fluorescence of the dye, and images of the

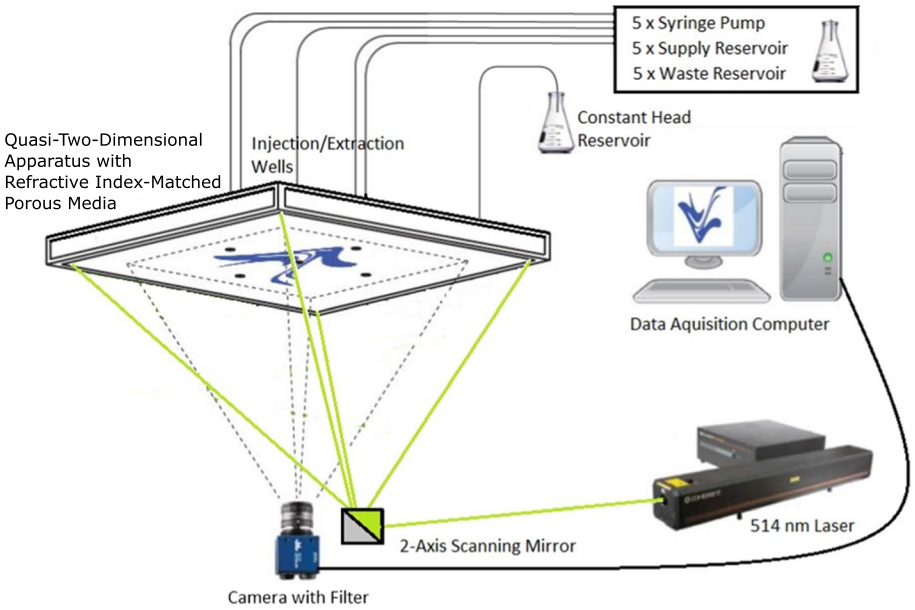

Fig. 1 Experimental setup

intensity of the dye fluorescence (surrogate for concentration) are captured by a camera. Details of each component of the setup are presented in this subsection.

2.2 Materials

Because the concentration measurements in the experiments were made using LIF, an optical technique, the porous media and fluid used in the experiments were required to be a refractive index-matched (RIM) pair. The selection of the RIM pair was based on several criteria. The RIM pair had to be safe, economical, non-reactive, and provide suitable optical clarity and minimal distortion through an imaging depth equal to the depth of RIM porous media in the apparatus, approximately 3.5 cm. Given these constraints and based on the study of Wright et al. (2017), borosilicate glass beads were chosen as the porous media. The beads are available in sizes from 1–8 mm and are scratch resistant, which allows for the cleaning and reuse of the porous media. Critically, borosilicate glass has a relatively low index of refraction at 1.474, making available a number of candidate RIM fluids. Glass beads of 3 mm nominal diameter (Pyrex, part# 7268–3) were chosen because this was the smallest size that could be loaded into a predetermined hexagonal close pack geometrical structure with a reasonable amount of effort, and 1-mm beads are available for use as a wall effect mitigation technique material (see Sect. 2.1.3).

Glycerin was chosen as the fluid. At room temperature, it matches the refractive index of borosilicate glass. Large volumes of working fluid were required, on the order of 10 L per experiment. So, a working fluid that did not require additional mixing was a key benefit. Glycerin is also less expensive than any other fluid with refractive index 1.474, exhibits superior chemical compatibility (i.e., it is non-reactive with most other chemicals, including those used in this study), is non-flammable, and carries with it no health advisories. Glycerin is relatively viscous, 1.41 kg m^{-1} s^{-1} at 20° C (Miner and Dalton 1953), three orders of magnitude higher than the viscosity of water at 20 °C (Finnemore and Franzini 2002).

The glycerin/Pyrex bead RIM pair was tested for temperature sensitivity, optical distortion, and maximum probe depth for a coherent laser sheet. These data supply information about the maximum allowable depth of RIM porous media. It was found that the typical range of ambient temperature in the laboratory, 21–24 °C, was suitable for providing a refractive index match that allowed an incident laser beam to remain collimated through the thickness of the apparatus. Specifically, for the depth-averaged imaging technique used in experiments (see Sect. 2.1.4), the RIM clarity should contribute to an image resolution fine enough to resolve depth-averaged concentrations at a scale smaller than one bead diameter. This target resolution was chosen in order to allow imaging of preferential flows within the bulk porous media. Tests conducted on the RIM pair and Rhodamine 6G dye confirm that high clarity images with minimal distortion can be obtained through 13 layers of HCP beads, equivalent to the imaging depth used in experiments (see Supplemental Information Fig. S2).

The solute used in the experiments was Rhodamine 6G (Aldrich, CAS# 989–38-8), a fluorescent dye that is soluble in glycerin. The fluorescence characteristics of Rhodamine 6G were tested at different dye concentrations to ensure a linear relationship between dye concentration and fluorescence intensity. Rhodamine 6G was chosen as the primary dye for the experiments due to its common use in other LIF experiments (Crimaldi 2008). Rhodamine 6G has a peak stimulation wavelength near 525 nm and a peak emission wavelength near 560 nm (Crimaldi 2008). Note that at 20° C, diffusivity for Rhodamine 6G

dye in glycerin is 1.9×10^{-9} cm^2 s^{-1} (Roth et al. 2020). The low diffusivity in relation to experimental run times of approximately 2 h will tend to minimize any diffusion in these experiments.

The dye stock solution was prepared by adding 8 mg of dye powder per liter of glycerin. Mixing was performed within an Erlenmeyer flask with a magnetic stir bar and stir plate. As compared with water, the relatively high viscosity of glycerin prevents turbulence, retarding mixing. Consequently, the glycerin was heated to approximately 30 °C during stirring, approximately halving the viscosity to 0.6 kg m^{-1} s^{-1}. Solutions were considered well mixed after continuous stirring for three days.

2.2.1 Apparatus

The quasi-two-dimensional apparatus is shown in Fig. 2. Novel aspects of the apparatus include a large study area made possible by the use of wall effect mitigation treatments to the top and bottom walls, making the flow representative of an unbounded porous media system. The apparatus was designed to make Darcy scale measurements of dye concentration within relatively homogeneously packed, 3-mm-diameter, monodisperse, spherical beads. Overall dimensions of the apparatus were approximately 50 cm × 50 cm × 4.4 cm (total volume of approximately 11,000 cm^3), corresponding to approximately 160 × 160 × 15 bead diameters. During experiments, dye was typically confined to the volume contained within the test section, a 23.2 cm × 23.2 cm × 3.5 cm region of interest within the center of the apparatus bounded by the imaging window on the bottom and the first layer of opaque beads on the top (see Fig. 2). Data collected from outside of the test section were not considered during analysis. The apparatus was packed with 13 layers of RIM beads and then 3 layers of opaque beads (see Sect. 2.1.3). Dye concentration measurements were averaged over the vertical thickness of RIM porous media, 3.5 cm, making this a quasi-two-dimensional apparatus.

The apparatus included five fully penetrating injection and extraction wells—one center well, with four equally spaced wells in a diamond pattern around the center well

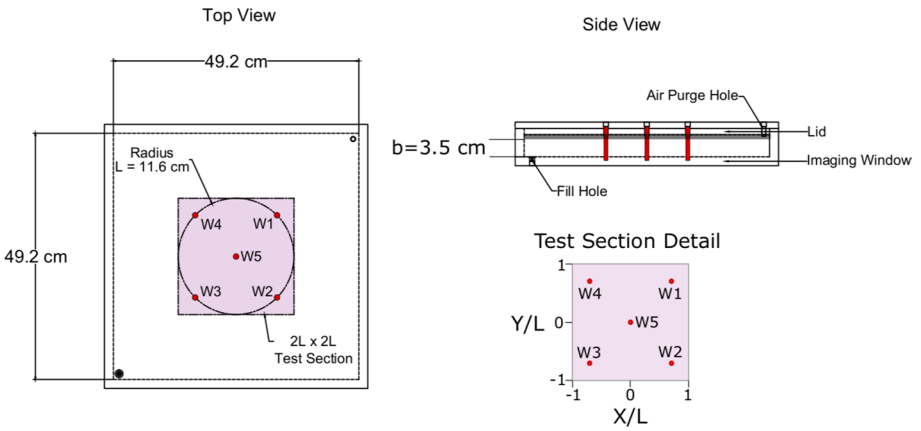

Fig. 2 Fabrication drawings of engineered injection and extraction apparatus. Wells 1–5 are marked in red, L is the radius from center well 5 to the surrounding wells. The test section is the volume shaded in pink, with dimensions of 2L x 2L x b (equivalent to 23.2 cm × 23.2 cm × 3.5 cm). The test section detail shows axis labels which apply to the plume images in Figs. 5, 6, 7, and 8

at a distance of $L = 11.6$ cm (37 bead diameters) from the center well (Fig. 2). Wells were fabricated from perforated tubing (Perforated Tubes Inc., code 70) with outer diameter 6.35 mm, wall thickness 0.635 mm, and perforations of diameter 1.3 mm, giving an overall open area of 66%. In order to further increase the open area, additional 1.3-mm holes were drilled into the perforated tubing, further increasing the open area to approximately 70% without compromising the structural integrity of the tubing against deformation by the porous media under the demands of the experiments. To ensure uniform flow over the apparatus depth, the wells were fully penetrating, with perforations along their entire length, which allowed fluid to flow freely, with minimal head loss compared to the head loss from the surrounding porous media. Injections and extractions through these wells rendered quasi-two-dimensional flow in a horizontal plane.

2.2.2 Bead Packing

Approximately homogeneous porous media packing was critical so that solute transport was controlled mainly by fluid injection and extraction through the wells rather than by heterogeneity. The porous media was packed with hexagonal close packing (HCP), which has a structurally stable geometry and corresponds to maximum density and minimum porosity for monodisperse spheres (Smith et al. 1929). Therefore, porosity could be used as a proxy for homogeneity within the porous media. The monodisperse Pyrex glass beads used in the experiments could be considered to have a more homogeneous packing as porosity approached the theoretical porosity of 0.26 for HCP (Smith et al. 1929).

While spherical beads naturally orient themselves in an HCP geometry, the occasional bead will become misaligned, disrupting the alignment of neighboring beads and eventually causing non-ideal packing for sequentially placed beads in the system. Therefore, care must be applied to bead placement. Considering that the apparatus contained approximately 500,000 beads, placing individual beads was not feasible. A technique involving layer-by-layer bead placement, followed by gentle shaking, was developed. This technique exploited each bead's proclivity toward self-alignment within an HCP lattice and was aided by the flat, parallel walls of the apparatus. HCP orientation was visually confirmed for each layer before adding additional beads. A total of 16 layers of 3-mm beads were packed into the apparatus. The manufacturer states that bead diameter is ± 0.75 mm of 3 mm. As measured by a random sample of 50 beads, there was a variance from the nominal 3 mm diameter of ± 0.2 mm. As such, beads that were visually determined to be larger or smaller than the nominal diameter were excluded during packing.

The top and bottom walls of the apparatus (parallel to flow) used wall effect mitigation techniques, designed to provide approximately uniform porosity up to the apparatus walls, which in turn prevents preferential flow near the walls (Fig. 3). On the bottom wall, where optical access was required, 1-mm beads (Chemglass, part# CG-1101–06) were placed against the wall in the pore space between three 3-mm beads. On the top wall, where optical access was not required, the top layer of 3-mm beads was pressed into a layer of wet silicone (General Electric, 100% Silicone II, Black) that submerged the upper 1.5 mm. Details on both wall effect mitigation techniques are provided in Roth et al. (2020), who showed that both mitigation techniques effectively eliminated preferential flow along the walls. Though the hemisphere-in-silicone wall effect mitigation technique (Fig. 3) proved effective in tests reported elsewhere (Roth et al. 2020), there was a chance that bead HCP configuration could be misaligned upon installation of the lid. Accordingly, the top three of the 16 layers were opaque beads, so any irregularities in flow near the wall would not

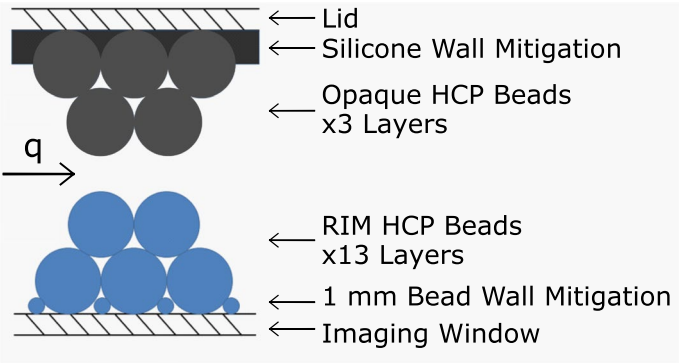

Fig. 3 Schematic of wall mitigation techniques. For the top wall, 3-mm beads are pressed into silicone, creating a layer of hemispheres. Three layers of HCP opaque beads are installed to further shield images from non-representative wall effects near the wall. RIM HCP beads constitute 13 layers of porous media over which data is collected. For the bottom wall, a sub-layer of transparent 1-mm beads is placed between the wall and the first layer of 3-mm beads, preserving optical access through the imaging window

be imaged during experiments, further ensuring porous media uniformity over the depth of the imaged domain.

2.2.3 Laser-Induced Fluorescence and Imaging

For these experiments, a LIF technique was developed to provide illumination approximately normal to the imaging window. By using this technique, the precision of LIF could be utilized within a relatively large porous media bed. A 514-nm laser beam produced by an argon-ion laser (Coherent, Innova 90C-6, Santa Clara, CA) was used to illuminate the fluorescent dye. To evenly illuminate the entire test section the laser beam was passed through a beam expander to produce a 1-cm-diameter beam. The expanded beam was then manipulated by reflection off of a two-axis galvo-mirror (Thorlabs, dual-axis scanning-galvo-mirror system, GVS312). A LabVIEW code directed the mirrors to sweep the beam over every point in the imaging window (the entire bottom face of the apparatus; see Fig. 2). Starting from the top, right corner of the imaging window, the beam scanned horizontally to the left, moved vertically down 0.25 cm, scanned horizontally to the right, moved 0.25 cm down, and continued until reaching the bottom left corner of the imaging window.

The apparatus allowed optical access only through the imaging window, so a camera (Imperx, Bobcat ICL-B1410M-SCO, Boca Raton, FL) was located beside the mirror to capture images of dye fluorescence (Fig. 1). The imaging window of the apparatus was located 2 m from the camera mount. The 2 m focal distance from the imaging window to the camera minimized parallax within captured images, with parallax of less than 1 bead diameter over the apparatus depth within the bounds of the test section, ensuring that the quasi-two-dimensional assumption was valid. Images were logged within an external computer, optimized for image capture (Boulder Imaging, Quazar, Boulder, CO). An optical band-pass filter (Omega Optics, 555DF30, Austin, TX), was attached to the camera lens, blocking the 514 nm excitation light from the laser while transmitting fluoresced light from the dye. The camera and scanning-galvo-mirror system were each controlled by a LabVIEW code which sent trigger signals to each component, communicated through an

intermediate data acquisition device (National Instruments, USB 6383, Austin, TX). The virtual shutter of the camera was opened, which initiated image capture. The synchronized galvo-mirror then rotated, sweeping the beam through the porous media domain. Upon completion of the beam sweep, exposure time for this single image was stopped by closing the camera's virtual shutter. The resulting image showed fluorescent emission intensity from the dye present within the laser sheet. Each image was captured using a one second exposure time, equal to the duration of one complete scan of the domain by the laser. Images were captured every 15 s, a sufficient frame rate to capture the transient fluid dynamics of the system for experiments with durations ranging from 120–150 min.

2.2.3.1 Fluid Handling Since glycerin is nearly incompressible, continuity demanded that the injected volume had to equal the extracted volume at every step of the injection and extraction sequence. The injections and extractions of glycerin through the five wells were controlled by a positive displacement plumbing system containing five high-accuracy syringe pumps (Kd Scientific, Legato 270, Holliston, MA) (Fig. 1). Each pump held four syringes (BD, 60 mL-Luer lock syringe, Franklin Lakes, NJ). For a single throw, two of the syringes injected fluid as the other two syringes simultaneously extracted fluid at an identical flowrate. The pumps were reversible and programmable, allowing continuous periodic injection and extraction. Since the combined volume of the two syringes supplying flow to injection or extraction was limited to 120 mL, a system of check valves was designed to fill the extracting syringes with source fluid as the injecting syringes supplied flow to the apparatus wells. The syringe pumps were programmed to instantaneously change direction once the extracting syringes had been completely filled, so that the former extraction syringes could then supply the wells and the former injection syringes could then draw from the fluid source. Three-way valves were also added to the plumbing loop, allowing for the selection of injection or extraction for the specific well (Supplemental Information Fig. S1). The system was designed to minimize the volume of recycled fluid by the system, such that fluid drawn from a well was not re-injected later in the experiment. Valves were linked with transparent, semi-rigid poly-vinyl chloride (PVC) tubing (Vyplas, part# TDX73-CAO, Flippin, AR).

After extensive testing by measurement of eluted volume through the pumping system, corrections were made for hydraulic capacitance caused by tubing elasticity and check valve triggering volume. In order to ensure that fluid injections and extractions were precise, corrected pumping rates were programmed into the syringe pumps. Further volumetric testing of the system confirmed acceptable accuracy, with experimental uncertainty less than 0.3% between tests. With the potential for a 0.3% volumetric pumping uncertainty in mind, the apparatus was designed with a constant head reservoir, allowing the apparatus to maintain constant pressure regardless of volumetric flux. The constant head reservoir also served as a surge tank, eliminating the potential for apparatus rupture.

2.2.4 Experimental Procedures

Prior to an experiment, new fluid (glycerin) was cycled through the pumping system, ensuring that all air was purged from the system. Triplicate background images of the porous media were captured through the imaging window without dye, in order to record the light from sources other than the dye, to be averaged and used for post-experiment image processing (see Sect. 2.2.1). Next, the dye plume was introduced to the flow cell as follows. 20 mL of dye solution was collected from the stock solution using

a 60 mL syringe fitted with a quick release valve that coupled with the well inlets. The apparatus was temporarily disconnected from the pumping system. The syringe containing the dye was then connected to the center well and dye was slowly injected at a rate of approximately 4 mL/min, creating an approximately cylindrical plume and expelling clear fluid to waste through the surrounding wells.

Prior to the start of the pumping sequence, all wells were then reconnected to the pumping system and the valve for the constant head reservoir was opened. The syringe pump and valves for the center well were opened, and 7 mL of dye-free glycerin was injected into the well to clear remaining dye from the plumbing directly upstream from the well. At this point, the resulting dye plume represents the initial condition for subsequent pumping steps.

The experiments were run with two different pumping sequences to observe the dye plume movement under time-varying flows. For each sequence, the volumes injected into each well are shown in Table 1 for each step. The volumes are given in terms of pore volumes of the test section, which has a pore volume of 583 mL. Each step lasted for a duration of 30 min. Both sequences were run in replicate to evaluate the repeatability of the experiments.

The first sequence is a push–pull sequence in which glycerin was alternately injected and extracted at the center well (Well 5 in Fig. 2) over four steps to create essentially radial flow in the vicinity of the dye plume, for a total of two injection steps and two extraction steps. In order to maintain conservation of mass of glycerin in the apparatus at each step, small amounts of glycerin were alternately extracted and injected at the four outer wells (Wells 1–4 in Fig. 2).

The second sequence is a stretching–folding sequence in which the dye plume was shifted to be positioned between Wells 4 and 5 (see Fig. 2) and then stretched and folded around a stagnation point near Well 5. This was followed by a second shift to reposition the plume between Wells 3 and 5 and then subsequently to stretch and fold the plume around a different stagnation point near Well 5.

To carry out the pumping sequences, pumps were programmed and three-way valves were set to the desired configurations for the first step in the sequence. Image capture and pumping were then started. Upon completion of the first step of the pumping sequence, image capture was stopped, pumps were reprogrammed, and valve

Table 1 Pore volumes eluted per step

	Well 1	Well 2	Well 3	Well 4	Well 5
Push–pull sequence					
Step 1	− 0.039	− 0.039	− 0.039	− 0.039	0.154
Step 2	0.013	0.013	0.013	0.013	− 0.051
Step 3	− 0.013	− 0.013	− 0.013	− 0.013	0.051
Step 4	0.006	0.006	0.006	0.006	− 0.026
Stretching–folding sequence					
Step 1	0	0.283	0	− 0.283	0
Step 2	0	− 0.565	0	0.452	0.113
Step 3	0.141	− 0.028	0.141	− 0.254	0
Step 4	0.283	0	− 0.283	0	0
Step 5	− 0.437	0	0.262	0	0.175

configurations were selected for the next step of the sequence. Image capture was reinitiated and pumps were started.

Upon completion of all steps of a pumping sequence, the apparatus was cleaned as follows to prepare for another experiment. The pumps and valves were set to extract fluid (dye and glycerin) from the center well, while dye-free glycerin was injected through the surrounding wells. Fluid was drawn from the center well until no dye remained in the imaging window. By extracting all dye from the apparatus, subsequent experiments could be performed using an identical porous media configuration.

Upon completion of all experiments, the cell was completely flooded with dye and imaged to record the dye-saturated intensity, which was used in post-experiment image processing (see Sect. 2.2.1) and to make a porosity map (see Sect. 2.2.2). Finally, the apparatus was drained of fluid, the lid was opened, and the total volume of beads was measured to calculate the average porosity (see Sect. 2.2.3).

2.3 Data Analysis

2.3.1 Image Processing

Post-experiment image processing procedures were developed specifically for use with the LIF in RIM porous media techniques used in these experiments. The raw LIF images captured during the experiment record light intensity $R(i,j)$ at each pixel (i,j) on a grid of 1040 by 1392 pixels. Note that this image included the entire apparatus, but most analysis was performed on data within the test section, corresponding to the central 485 by 485 pixels of the image. The recorded light intensity includes both light fluoresced from the dye, $I(i,j)$, and background artifacts from unwanted light in the laboratory and from attenuated laser light transmitted through the camera filter. Thus, the light intensity from the dye, $I(i,j)$, is found by

$$I(i,j) = R(i,j) - B_R(i,j) \tag{1}$$

where $B_R(i,j)$ is the intensity in a background image taken prior to the injection of dye (see Sect. 2.1.6). In order to reduce experimental uncertainty caused by variations in laser intensity or camera noise, image $B_R(i,j)$ is the average of triplicate background images collected sequentially under the same conditions at the same time during the experiment.

The recorded intensity is also affected by the structure of the porous media. Each pixel represents an identical sample volume, equal to the product of pixel area and the imaging depth. The sample volume comprises beads, where no dye can be present, and pore space, which can contain dye. Since pixels are smaller than the projected area from a bead, the total pore volume within each pixel is different, leading to variations in dye emission intensity that are not caused by variations in dye concentration. Therefore, a relative intensity image, i.e., measured intensity at each pixel relative to the maximum possible intensity at each pixel, is created. The maximum intensity, $I_o(i,j)$, at a pixel is given by

$$I_o(i,j) = S(i,j) - B_S(i,j), \tag{2}$$

where $S(i,j)$ is the dye-saturated intensity image (described in Sect. 2.1.6) and $B_S(i,j)$ represents the background artifacts that must be removed. Note that $B_R(i,j)$ and $B_S(i,j)$ both represent background intensity images; however, they do not necessarily represent the same image. A background intensity image is taken prior to the dye injection of each experiment, so each experiment has a different $B_R(i,j)$, which is subtracted from the raw intensity

images $R(i,j)$ to obtain the fluorescence intensity images $I(i,j)$. The dye-saturated intensity image $S(i,j)$ is taken only after all of the experiments are completed; therefore $B_S(i,j)$ is equivalent to $B_R(i,j)$ of the last experiment. In order to reduce experimental uncertainty, images $S(i,j)$ and $B_S(i,j)$ are each the average of triplicate images collected sequentially under the same conditions at the same time during the experiment.

For dye at sufficiently low concentration, dye concentration is linearly proportional to the normalized fluorescence intensity $I(i,j)/I_o(i,j)$. In this work, we are interested in the relative dye concentration, $C_R(i,j)$, (relative to the concentration of dye in the injected dye solution, C_o, which, from Sect. 2.1.1, is 8 mg/L), which is given by

$$C_R(i,j) = \alpha \frac{I(i,j)}{I_o(i,j)} = \alpha \frac{R(i,j) - B_R(i,j)}{S(i,j) - B_S(i,j)}, \tag{3}$$

where α is a constant of proportionality that is found by ensuring that the total mass of dye, M_T, in the apparatus at any time is equal to the mass of dye, M_{inj}, injected prior to the start of the pumping sequence. The mass of dye injected is $M_{inj} = C_o V_o$, where $C_o = 8$ mg/L (equivalent to 8 µg/mL) and $V_o = 20$ mL is the volume of dye injected into the apparatus prior to the start of the pumping sequence. Thus, assuming uniform flux throughout the full depth of the center injection well, the mass injected into the test section will be proportional to its depth of 3.5 cm out of the full depth of 4.4 cm, giving $M_{inj} = 0.13$ mg (note that the height of the test section does not include the opaque beads). The total mass M_T in the apparatus can be obtained by summing the masses, $M(i,j)$, in each pixel, given by

$$M(i,j) = bAC_o C_R(i,j) n(i,j) \tag{4}$$

where $b = 3.5$ cm is the thickness of RIM porous media in the apparatus, $A = 0.0023$ cm^2 is the area of a pixel, $C_o = 8$ mg/L, C_R is given by (3), and $n(i,j)$ is the porosity of pixel (i,j) (see Sect. 2.2.3). Using (3) and (4), the total mass M_T is given by

$$M_T = \sum_i \sum_j M(i,j) = bAC_o \sum_i \sum_j C_R(i,j) n(i,j) = \alpha bAC_o \sum_i \sum_j \frac{I(i,j)}{I_o(i,j)} n(i,j) \tag{5}$$

Thus, the constant of proportionality, α, is found by setting the M_T in (5) equal to M_{inj}. Dye was injected into the apparatus through the center well and then mostly cleared from the well by injection of fluid with no dye during step 0 of each sequence, although trace amounts of dye could remain. Any such remaining traces of dye still present within the well would be cleared during subsequent pumping steps. Therefore, the constant α is calculated using the maximum value of M_T present during the pumping sequence, after all dye has been cleared from the center well.

Image-to-image intensity variations, mostly attributable to camera noise, across triplicate background images were very small compared to those across the triplicate images averaged to make the saturated image, $S(i,j)$, which were mostly attributable to laser intensity fluctuation. Noting that $S(i,j)$ was used to calculate $C_R(i,j)$, the experimental uncertainty from saturated images propagates systemically through the data. Experimental uncertainty was determined by analysis of aggregate image intensity variation across each of the triplicate images, $S^k(i,j)$, where superscript k denotes the triplicate number. Experimental uncertainty percentage, ε, is estimated by

$$\varepsilon = 100\left(\max\left| \frac{\sum_i \sum_j S^k(i,j) - \sum_i \sum_j S(i,j)}{\sum_i \sum_j S(i,j)} \right| \right), \text{for } 1 \le k \le 3. \tag{6}$$

2.3.2 Bulk Porosity

The average porosity, n_{ave}, of the porous media was calculated as

$$n_{ave} = \frac{V_t - V_s}{V_t} \tag{7}$$

where V_t is the volume of the bead-containing cavity and V_s is the volume of the beads. The volume of the beads was measured after all experiments were completed using the following approach. The apparatus lid was taken off, and all beads were carefully removed, ensuring that no beads were lost. The beads were thoroughly washed in water to remove all glycerin, rinsed with de-ionized (DI) water to ensure no precipitates formed on the bead surface, and covered with a lint-free cloth and allowed to dry. A known volume of DI water was poured into a volumetric flask. Once the beads were dry, they were added to the flask. To ensure that no air was entrapped in the beads, the flask was vibrated upon addition of the beads. The total volume of beads, V_s, was equal to the displaced volume of DI water.

The wall effect mitigation technique used on the apparatus lid included a layer of silicone with one layer of beads embedded within that silicone. Consequently, the volume of the apparatus could not be found by computation of apparatus dimensions. To measure V_t, the beads that were embedded in the silicone were left in place. Before measuring apparatus volume, we ensured that the embedded beads comprised a mono-layer by brushing off beads (to be measured as the bulk porous media) that were only partially connected to the silicone. The remaining beads were then considered to be integrated within the silicone, with no pore space between the beads and the silicone. With the bulk porous media removed, the apparatus volume, V_t, was then measured by adding water to the apparatus with the silicone and embedded beads in place. Note that V_t includes 13 layers of transparent beads as well as 3 layers of opaque beads.

2.3.2.1 Porosity Distribution A map of the spatially varying porosity distribution $n(i,j)$ was created to solve (5), but also to provide critical information about heterogeneity within the porous media field. This novel mapping technique was performed by determining the porosity at each pixel within the test section. As described in Sect. 2.2.1, the pore volume at a pixel is proportional to the maximum intensity, $I_o(i,j)$, at a pixel, which is a measure of fluorescence intensity controlled by the ratio of void space (filled with dye) to total volume (including solids which contained no dye). Thus, spatially varying porosity is given by.

$$n(i,j) = \lambda I_o(i,j) \tag{7}$$

where λ is a constant of proportionality defined such that the average of $n(i,j)$ is equal to n_{ave} (calculated in Sect. 2.2.2), i.e.,

$$\lambda = \frac{n_{\text{ave}}}{\frac{1}{N}\sum_i \sum_j I_o(i,j)} \tag{9}$$

where N is the total number of pixels. The creation of a porosity map is a novel approach developed for these experiments.

2.3.3 Comparison of Replicates

To evaluate the similarity in the overall geometry of the plumes across replicate experiments, we calculated and compared the locations of the centroids, the spread of the plume around the centroid, and the volume occupied by the plume. We also compared replicates with a statistical metric, the two-dimensional correlation coefficient.

The centroids were calculated over a region covering 485 × 485 pixels centered at Well 5. Let the Cartesian coordinate axes be defined such that the x direction is along the rows of pixels (i) and the y direction is along the columns of pixels (j) with the origin at Well 5. Then, the centroids, $\bar{x}$ and $\bar{y}$, in x and y, respectively, are given by

$$\bar{x} = \frac{\sum_i \sum_j x(j) M(i,j)}{M_T} \tag{10}$$

$$\bar{y} = \frac{\sum_i \sum_j y(i) M(i,j)}{M_T} \tag{11}$$

where $x(j)$ and $y(i)$ are x and y coordinates of the center of the pixel in the jth column and in the i^{h} row, respectively.

The spread of the plume about the centroid was quantified as the normalized mass moment of inertia, I, given by

$$I = \frac{\sum_i \sum_j r(i,j)^2 M(i,j)}{L^2 M_T} \tag{12}$$

where $r(i,j)$ is the distance from the plume centroid to pixel (i,j) and $L = 11.6$ cm is the distance between Well 5 and all other wells.

The volume occupied by the plume was quantified by the reactor ratio, R_R, given by (Kitanidis 1994)

$$R_R = \frac{E}{E_{\max}} \tag{13}$$

where E is the dilution index given by (Kitanidis 1994)

$$E = Ab \exp\left(- \sum_i \sum_j P(i,j) \ln \left[P(i,j) \right] \right) \tag{14}$$

where A is the area of a pixel, b is the thickness of the apparatus, and $P(i,j) = M(i,j)/M_T$. In (13), $E_{\max}$ is the maximum dilution index possible within the volume of interest. For these experiments, the volume of interest is defined as the volume of the test Sect. (583 mL) centered on the center well with dimensions of 23.2 cm × 23.2 cm and thickness equal to that of the RIM porous media in the apparatus ($b = 3.5$ cm).

Turning now to the statistical metrics, we calculated the two-dimensional correlation coefficient, ρ, for corresponding plume images using the corr2 function in MATLAB, given by

$$\rho = \frac{\sum_i \sum_j \left(C_{R1}(i,j) - \overline{C_{R1}}\right)\left(C_{R2}(i,j) - \overline{C_{R2}}\right)}{\sqrt{\left[\sum_i \sum_j \left(C_{R1}(i,j) - \overline{C_{R1}}\right)^2\right]\left[\sum_i \sum_j \left(C_{R2}(i,j) - \overline{C_{R2}}\right)^2\right]}}, \tag{15}$$

where the subscripts 1 and 2 refer to the experimental replicate number, and $\overline{C_{R1}}$ and $\overline{C_{R2}}$ are the mean values of all pixels within the image from replicates 1 and 2, respectively. The correlation coefficient is used to quantify similarities between data sets by plotting them against each other and then considering the slope of a best fit line in conjunction with data divergence from that line. A perfect match between data sets would be described by a correlation coefficient equal to unity.

3 Results

This section reports the average porosity and the porosity distribution. This section also presents dye concentrations for each step of each replicate of both pumping sequences and provides quantitative analyses of the replicate images to demonstrate the high degree of reproducibility. This section also presents the results of the two-scalar protocol and demonstrates the validity of the approach. Experimental uncertainty calculated from (6) is $\varepsilon = 0.05\%$; thus the following data are subject to an estimated uncertainty of $\pm 0.05\%$.

3.1 Porosity

The average porosity was calculated using (7), with V_t and V_s measurements of 10,125 cm^3 and 6980 cm^3, respectively, following the approach described in Sect. 2.2.2. It should be noted that the apparatus contains 13 layers of transparent beads with a depth of approximately 3.5 cm and a volume of approximately 8500 cm^3. However, to eliminate wall effects near the lid, we also included 3 layers of opaque beads, bringing the overall depth to approximately 4.3 cm. Bulk porosity measurements included both transparent and opaque beads, so $V_t \approx 49.2\ \text{cm} \times 49.2\ \text{cm} \times 4.3\ \text{cm} = 10{,}400\ \text{cm}^3$. This volume includes approximately 275 cm^3 for the volume of each well and the bead volume embedded in the silicone, giving the reported porous media volume of 10,125 cm^3.

Using the measured values of V_t and V_s, we obtain $n_{\text{ave}} = 0.31$, which is slightly higher than the minimum theoretical porosity of 0.26 for HCP. The measured porosity is expected to be higher than the theoretical minimum because of non-uniform bead size and because the apparatus geometry does not exactly match aggregate HCP bead geometry. Nevertheless, to our knowledge, this is the lowest reported measured porosity for (nearly) monodisperse spheres. Schwartz and Smith (1953) reported a porosity of 0.32, measured within the central volume of an experimental test section, without contact with apparatus walls, making it difficult to compare their result to our system-wide porosity measurements within the apparatus as a whole. Also, Eisfeld and Schnitzlein (2001) reported a porosity of 0.348, but beyond these two examples, for the large majority of experiments, porosity is typically very near 0.4 (Atmakidis and Kenig 2015; Carman 1937; Cohen and Metzner 1981; Eisfeld and Schnitzlein 2001; Fand et al. 1987; Gunn 1987; Lee et al. 2018; McWhirter et al. 1998; Muhammad and Massimo 2017; Rolle et al. 2009). Thus, the meticulous bead packing procedure described in Sect. 2.1.3 in conjunction with a relatively precise degree of

monodispersivity produces a porosity that is quite close to the theoretical minimum porosity for HCP, indicating relatively homogeneous packing.

The porosity map (Fig. 4) was created from (8) using the maximum intensity image $I_o(i,j)$ and $\lambda = 1.93 \times 10^{-4}$ obtained from (9). Porosity falls within the range of 0.28 to 0.38, which is between the theoretical minimum porosity of 0.26 for HPC and the expected random close pack porosity of 0.4 (Smith et al. 1929). This porosity distribution was used in (5) to calculate the mass of dye and can also be used to gauge the degree of homogeneity achieved for the porous media packing. Areas with a high degree of homogeneity are indicated by a relatively uniform porosity distribution in the map (Fig. 4a). For the more homogeneous regions, porosity is near 0.28, which is close to the theoretical limit of 0.26 for HCP. The porosity map also shows veins of higher porosity, where porosity ranges between 0.32 and 0.38 (Fig. 4b).

3.2 Concentration Images for Single-Scalar Experiments

Figures 5 and 6 show the dye concentrations for each step of the push–pull and stretching–folding sequences, respectively. For each sequence, replicate experiments were conducted and both sets of results are shown in the figures. As expected, the push–pull scenario moves the plume radially outward in steps 1 and 3 and radially inward in steps 2 and 4. Also as expected, the stretching–folding scenario manifests qualitatively different behavior, shifting the plume between the wells (steps 1, 3, and 4) and then bending it around a stagnation point (steps 2 and 5) to create a horseshoe shape. Note that the repositioning in step 4 effectively smears the two branches of the horseshoe that were present at the end of step 3, so step 5 produces a more diffuse horseshoe.

Qualitative analysis of plume dynamics for the push–pull and single-scalar stretching–folding sequences (Figs. 5 and 6) indicates good agreement for the shape and spread of the plume in the replicate experiments, including the diffuse horseshoe at the end of step 5 in the stretching–folding sequence. Fine-scale structures within the plumes appear to be identical across replicate experiments, as well as overall plume distribution. Mass was essentially conserved through all experiments (Supplemental Information Table S1). The total mass M_T calculated by (5) varied by 3.2% and 3.6% over the course of the push–pull

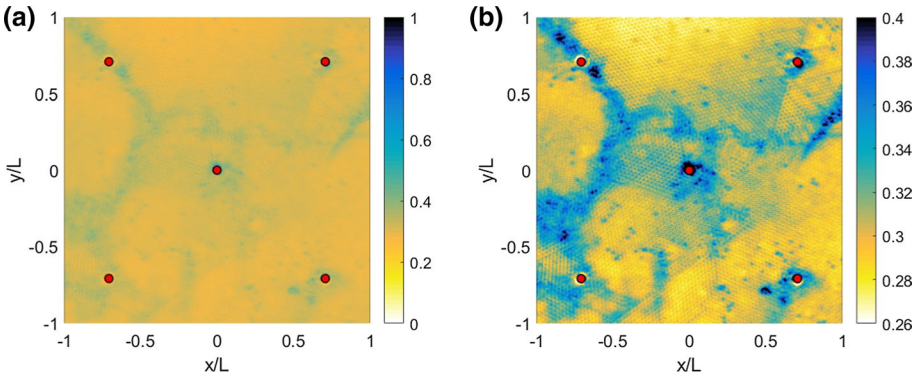

Fig. 4 Porosity map. *a* Color scale from $n=0$ to $n=1$ to illustrate the overall degree of homogeneity. *b* Color scale from $n=0.28$ to $n=0.4$ to accentuate the local heterogeneity. Red circles represent wells. Note that the x and y directions correspond to the i and j pixel directions, with Well 5 located at $(x,y)=(0,0)$. $L=11.6$ cm is the separation distance between Well 5 (center well) and each outer well

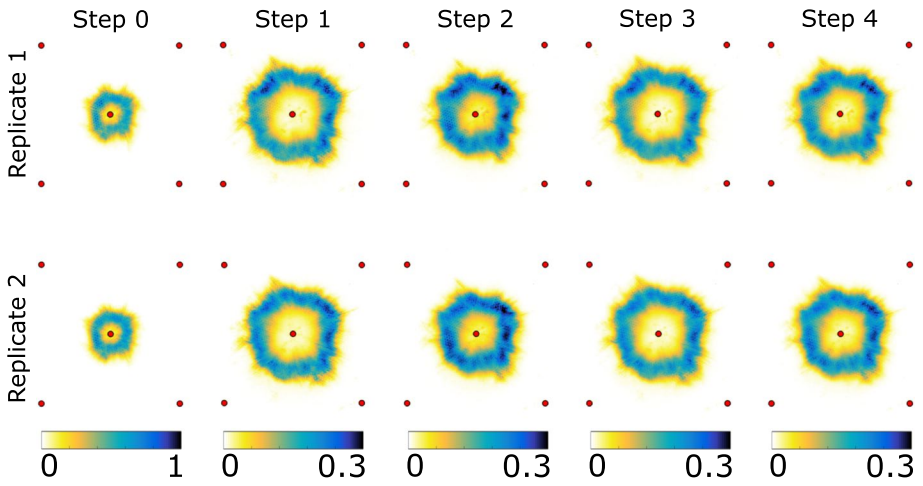

Fig. 5 Distributions of relative concentration, C_R, at the end of each step of the push–pull experiment 1 (top row) and push–pull replicate experiment 2 (bottom row). Red dots represent well locations. The constant of proportionality in (3) is $=0.565$ and 0.466 for replicates 1 and 2, respectively. Note the plot region is the test section as shown in Fig. 2

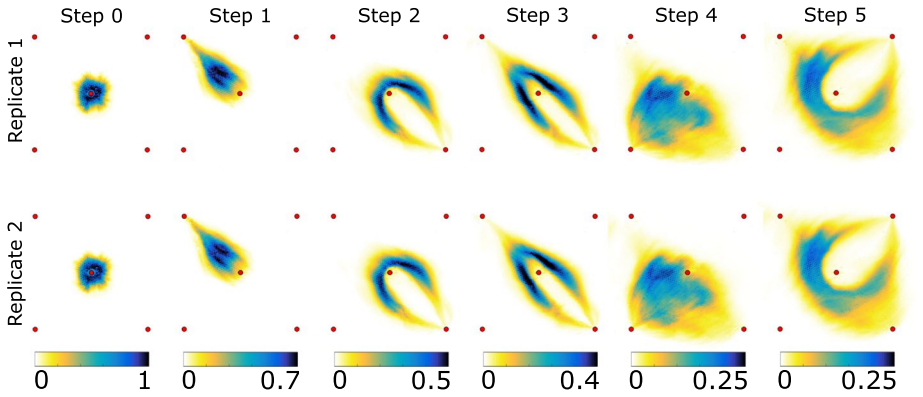

Fig. 6 Distributions of relative concentration, C_R, at the end of each step of stretching–folding replicate 1 (top row) and stretching–folding replicate 2 (bottom row). Red dots represent well locations. The constant of proportionality in (3) is = 0.600 and 0.576 for experiments 1 and 2, respectively. Note the plot region is the test section as shown in Fig. 2

experiments for replicates one and two, respectively; the total mass varied by 0.9% and 1.5% over the course of the stretching–folding experiments for replicates one and two, respectively. All changes in mass are attributable to scalar extraction through the wells during the sequence.

The centroids, mass moment of inertia, and reaction ratio are shown in Table 2 for each step of each experiment. Comparisons of these measures between replicate experiments are shown in Table 3. For the centroid location, Table 3 shows the normalized distance between the centroids of the plumes, ΔC, of the two replicate experiments, normalized by the square root of the average initial plume areas of the replicates, A_{Plume}.

Table 2 Spatial statistics of plumes for each step of each replicate of each experiment

Experiment	Step number	Centroid, $(\bar{x}/L, \bar{y}/L)$	Normalized moment of inertia, I	Reactor ratio, R_R
Push–Pull Replicate 1	0	0.023, 0.002	$5.10*10^{-6}$	0.092
	1	0.022, 0.010	$1.38*10^{-5}$	0.253
	2	0.027, 0.012	$1.04*10^{-5}$	0.215
	3	0.025, 0.014	$1.38*10^{-5}$	0.257
	4	0.027, 0.016	$1.12*10^{-5}$	0.238
Push–Pull Replicate 2	0	0.017, 0.002	$4.63*10^{-6}$	0.085
	1	0.019, 0.008	$1.33*10^{-5}$	0.244
	2	0.023, 0.009	$9.98*10^{-6}$	0.206
	3	0.022, 0.011	$1.32*10^{-5}$	0.228
	4	0.025, 0.013	$1.16*10^{-5}$	0.151
Stretching–folding Replicate 1	0	0.016, − 0.001	$3.39*10^{-6}$	0.058
	1	− 0.251, 0.230	$1.09*10^{-5}$	0.099
	2	0.101, − 0.085	$1.06*10^{-5}$	0.166
	3	0.012, − 0.015	$1.12*10^{-5}$	0.182
	4	− 0.201, − 0.219	$1.74*10^{-5}$	0.317
	5	− 0.015, − 0.016	$2.00*10^{-5}$	0.377
Stretching–folding Replicate 2	0	0.017, 0.001	$3.48*10^{-6}$	0.058
	1	− 0.248, 0.232	$1.11*10^{-5}$	0.097
	2	0.106, -0.083	$1.07*10^{-5}$	0.167
	3	0.025, − 0.016	$1.13*10^{-5}$	0.183
	4	− 0.188, − 0.219	$1.72*10^{-5}$	0.318
	5	0.003, − 0.017	$2.02*10^{-5}$	0.380

Table 3 shows the percent difference calculated from the reactor ratio values obtained in the experimental replicates and the percent difference in mass moments of inertia calculated from the normalized values obtained in the experimental replicates.

The difference in centroid location, ΔC, across replicates is less than 0.6 mm for all steps of the push–pull experiments and less than 2.3 mm for all steps of the stretching–folding experiments. Average area of the initial plume, A_{Plume}, for the push–pull and folding experiments was 37.1 cm^2 and 26.0 cm^2, respectively, giving normalized ΔC values of less than or equal to 0.01 and 0.04 for the experiments. The relative differences in moment of inertia are 3 – 9% for the push–pull experiments and 1–3% for the stretching–folding experiments. The relative difference in reactor ratios are 3–8% for the push–pull scenario and less than 2% for the stretching–folding scenario. In all cases, the differences are small. The larger differences shown in comparing the two push–pull experiments are likely due to slightly different initial conditions. Table 3 indicates that the replicate plumes in push–pull step 0 do not match as well as those found in the stretching–folding sequence. Although the push–pull scenario exhibits lower velocities, which would typically lead to enhanced variability due to molecular diffusion, the low

Table 3 Comparison of plume spatial statistics across replicate experiments

Experiments compared	Step number	ΔCentroid location ($\Delta C/A_{\text{Plume}}^{1/2}$)	Difference moment of inertia (%)	Difference reactor ratio (%)	Correlation coefficient, (ρ)
Push–Pull Replicates 1 vs. 2	0	0.010	9.21	8.26	0.985
	1	0.007	3.61	3.51	0.984
	2	0.009	3.89	4.61	0.986
	3	0.007	4.12	4.50	0.986
	4	0.008	3.38	4.06	0.987
Stretching–folding replicates 1 vs. 2	0	0.005	2.46	0.968	0.991
	1	0.009	2.36	1.42	0.994
	2	0.012	0.889	0.453	0.992
	3	0.029	1.13	0.823	0.988
	4	0.030	1.35	0.362	0.991
	5	0.041	0.599	0.816	0.990

diffusivity of Rhodamine dye in glycerin leads to the conclusion that inconsistencies between replicates likely propagate from the initial condition mismatch.

Correlation coefficients are shown in Table 3. Two-dimensional correlation coefficients are between 0.98 and 0.99 for the push–pull experiments and greater than 0.99 for the stretching–folding experiments (Table 3). These results confirm the reproducibility of the experiments.

The high degree of reproducibility is notable considering that the initial plume geometry, resulting from injection by hand, was not exactly reproducible between experiments. One might expect that differences in the initial condition could carry over into subsequent steps in each pumping sequence due to the minimal amount of diffusion present in this high Peclet number system. Even though the initial dye injection was responsible for some variability across experiments, it was not substantial. This suggests that plume evolution is controlled by the kinematics of the flow, or to use the language of dynamical systems, the plumes appear to be moving toward an attractor that depends on subsequent spatiotemporally varied flow forcings rather than initial plume geometry.

4 Conclusion

This study has reported improved RIM and LIF techniques that produced high-resolution data for a quasi-two-dimensional test section, within an apparatus designed to minimize wall effects and maximize reproducibility between experiments. These first-of-their-kind data sets showed the temporal and spatial evolution of solute plumes produced by two different pumping sequences (push–pull and stretching–folding). Data from these experiments can be used to investigate the physics of solute dispersion, spreading, and mixing in porous media. In particular, this study reported a number of specific improvements: (1) porous media packing for increased homogeneity, (2) improved imaging techniques in quasi-two-dimensional porous media experiments, (3) optical porosity mapping techniques, and (4)

implementation of wall effect mitigation measures. Porous media packing techniques of the spherical, monodisperse beads produced highly homogeneous bulk porous media that provided reproducible results with typical correlation coefficients near unity. Similarly, the improved LIF imaging techniques in RIM porous media allowed for the creation of novel porosity maps, which were calibrated with physical porosity measurements. Taken together, all of these techniques should prove valuable in the analysis of plume spreading phenomena in a diverse array of solute transport experiments. Experimental methods developed in this research could have applications to a number of fields beyond groundwater hydrology, including chemical engineering, biomedical research, or oil recovery, since a greater understanding of flow patterns through any porous media system is of paramount utility.

Supplementary Information The online version contains supplementary material available at (https://doi.org/10.1007/s11242-021-01545-x) contains supplementary material, which is available to authorized users.

Acknowledgements The authors would like to thank the anonymous referees for their thoughtful comments and suggested edits that have improved the rigor and presentation of this work. This research was funded by the National Science Foundation under Grants EAR-1417005 and EAR-1417017. The authors have no conflicts of interest to declare that are relevant to the content of this article.

References

Amini, N., Hassan, Y.A.: An investigation of matched index of refraction technique and its application in optical measurements of fluid flow. Exp. Fluids **53**, 2011–2020 (2012). https://doi.org/10.1007/s00348-012-1398-x

Atmakidis, T., Kenig, E.Y.: Numerical analysis of residence time distribution in packed bed reactors with irregular particle arrangements. Chem. Product Process Model **10**, 17–26 (2015). https://doi.org/10.1515/cppm-2014-0021

Budwig, R.: Refractive-index matching methods for liquid flow investigations. Exp. Fluids **17**, 350–355 (1994). https://doi.org/10.1007/bf01874416

Carman, P.C.: Fluid flow through granular beds. Trans. Inst. Chem. Eng. **15**, 150–166 (1937)

Chen, J.-D., Wada, N.: Visualization of immiscible displacement in a three-dimensional transparent porous medium. Exp. Fluids **4**, 336–338 (1986). https://doi.org/10.1007/bf00266299

Cohen, Y., Metzner, A.B.: Wall effects in laminar flow of fluids through packed beds. AIChE J. **27**, 705–715 (1981). https://doi.org/10.1002/aic.690270502

Crimaldi, J.P.: Planar laser induced fluorescence in aqueous flows. Exp. Fluids **44**, 851–863 (2008)

Edery, Y., Dror, I., Scher, H., Berkowitz, B.: Anomalous reactive transport in porous media: experiments and modeling. Phys. Rev. E **91**, 052130 (2015)

Eisfeld, B., Schnitzlein, K.: The influence of confining walls on the pressure drop in packed beds. Chem. Eng. Sci. **56**, 4321–4329 (2001). https://doi.org/10.1016/s0009-2509(00)00533-9

Fand, R.M., Kim, B.Y.K., Lam, A.C.C., Phan, R.T.: Resistance to the flow of fluids through simple and complex porous-media whose matrices are composed of randomly packed spheres. J. Fluids Eng-Trans Asme **109**, 268–274 (1987)

Finnemore EJ, Franzini JB (2002) Fluid mechanics with engineering applications vol 10. McGraw-Hill, New York

Fort C, Fu, C. D., Weichselbaum, N. A., Bardet, P. M.: Refractive index and solubility control of paracymene solutions for index-matched fluid–structure interaction studies. Exp. Fluids **56**: 210

Gunn, D.J.: Axial and radial dispersion in fixed-beds. Chem. Eng. Sci. **42**, 363–373 (1987). https://doi.org/10.1016/0009-2509(87)85066-2

Kree, M., Villermaux, E.: Scalar mixtures in porous media. Phys. Rev. Fluid **2**(10), 104502 (2017). https://doi.org/10.1103/PhysRevFluids.2.104502

Lee, J., Rolle, M., Kitanidis, P.K.: Longitudinal dispersion coefficients for numerical modeling of groundwater solute transport in heterogeneous formations. J. Contam. Hydrol. **212**, 41–54 (2018). https://doi.org/10.1016/j.jconhyd.2017.09.004

McWhirter, J.D., Crawford, M.E., Klein, D.E.: Magnetohydrodynamic flows in porous media II: experimental results. Fusion Technol. **34**, 187–197 (1998)
Miner CS, Dalton NN (1953) Glycerol. Reinhold Publishing Corporation
Muhammad, M., Massimo, R.: Experimental investigation of the impact of compound-specific dispersion and electrostatic interactions on transient transport and solute breakthrough. Water Resour. Res. **53**, 1189–1209 (2017). https://doi.org/10.1002/2016WR019727
Northrup, M.A., Kulp, T.J., Angel, S.M., Pinder, G.F.: Direct measurement of interstitial velocity field variations in a porous medium using fluorescent-particle image velocimetry. Chem. Eng. Sci. **48**, 13–21 (1993). https://doi.org/10.1016/0009-2509(93)80279-Y
Patil, V., Finn, J., He, X., Ziazi, R., Apte, SV., Liburdy, JA., Wood, B.: Experimental versus computational methods in the study of flow in porous media. In: ASME 2014 4th Joint US-European Fluids Engineering Division Summer Meeting collocated with the ASME 2014 12th International Conference on Nanochannels, Microchannels, and Minichannels, 2014. American Society of Mechanical Engineers, pp V01DT40A003-V001DT040A003
Rolle, M., Eberhardt, C., Chiogna, G., Cirpka, O.A., Grathwohl, P.: Enhancement of dilution and transverse reactive mixing in porous media: experiments and model-based interpretation. J. Contam. Hydrol. **110**, 130–142 (2009). https://doi.org/10.1016/j.jconhyd.2009.10.003
Roth, E.J., Gilbert, B., Mays, D.C.: Colloid Deposit morphology and clogging in porous media: fundamental insights through investigation of deposit fractal dimension. Environ. Sci. Technol. **49**, 12263–12270 (2015). https://doi.org/10.1021/acs.est.5b03212
Roth, E.J., Neupauer, R.M., Mays, D.C., Sather, L.J., Crimaldi, J.P.: Wall Effect mitigation techniques for experiments with planar walls. Transp. Porous Media **132**, 423–441 (2020). https://doi.org/10.1007/s11242-020-01399-9
Saleh, S., Thovert, J.F., Adler, P.M.: Measurement of two-dimensional velocity fields in porous media by particle image displacement velocimetry. Exp. Fluids **12**, 210–212 (1992). https://doi.org/10.1007/bf00188261
Schwartz, C.E., Smith, J.M.: Flow distribution in packed beds. Ind. Eng. Chem **45**(6), 1209–1218 (1953)
Saleh, S., Thovert, J.F., Adler, P.M.: Flow along porous media by partical image velocimetry. AIChE J. **39**, 1765–1776 (1993). https://doi.org/10.1002/aic.690391104
Smith, W.O., Foote, P.D., Busang, P.F.: Packing of homogeneous spheres. Phys. Rev. **34**, 1271–1274 (1929). https://doi.org/10.1103/PhysRev.34.1271
Stohr, M., Roth, K., Jahne, B.: Measurement of 3D pore-scale flow in index-matched porous media. Exp. Fluids **35**, 159–166 (2003). https://doi.org/10.1007/s00348-003-0641-x
Werth, C.J., Zhang, C., Brusseau, M.L., Oostrom, M., Baumann, T.: A review of non-invasive imaging methods and applications in contaminant hydrogeology research. J. Contam. Hydrol. **113**, 1–24 (2010). https://doi.org/10.1016/j.jconhyd.2010.01.001
Wright, S.F., Zadrazil, I., Markides, C.N.: A review of solid–fluid selection options for optical-based measurements in single-phase liquid, two-phase liquid–liquid and multiphase solid–liquid flows. Exp. Fluids **58**, 108 (2017). https://doi.org/10.1007/s00348-017-2386-y